3-18-2021

Enhanced Porosity in Self-Assembled Morphologies Mediated by Charged Lobes on Patchy Particles

Brunno C. Rocha
University of New Hampshire, Durham

Sanjib Paul
New York University

Harish Vashisth
University of New Hampshire, Durham, harish.vashisth@unh.edu

Comments
This is an Open Access article published by ACS Publications in Journal of Physical Chemistry B in 2021, available online: https://dx.doi.org/10.1021/acs.jpcb.0c11096

Recommended Citation
Brunno C. Rocha, Sanjib Paul, and Harish Vashisth. Enhanced Porosity in Self-Assembled Morphologies Mediated by Charged Lobes on Patchy Particles, J. Phys. Chem. B 2021, 125, 12, 3208–3215, https://doi.org/10.1021/acs.jpcb.0c11096

THE JOURNAL OF PHYSICAL CHEMISTRY B
A JOURNAL OF THE AMERICAN CHEMICAL SOCIETY

pubs.acs.org/JPCB

Article

Enhanced Porosity in Self-Assembled Morphologies Mediated by Charged Lobes on Patchy Particles

Published as part of The Journal of Physical Chemistry virtual special issue "Carol K. Hall Festschrift".

Brunno C. Rocha, Sanjib Paul, and Harish Vashisth*

Cite This: *J. Phys. Chem. B* 2021, 125, 3208–3215

Read Online

ACCESS | Metrics & More | Article Recommendations | Supporting Information

ABSTRACT: Colloidal patchy particles are particles with anisotropic "patches" decorating their surfaces. Several properties of these patches including their size, number, location, and interactions provide control over self-assembly of patchy particles into structures with desired properties. We report on simulation studies of particles where patches take the form of lobes. Based on the number and locations of lobes, these particles have different shapes (trigonal planar, square planar, tetrahedral, trigonal bipyramidal, and octahedral). We investigated the effect of incorporating charges on the lobes in achieving porous self-assembled morphologies across a range of temperatures. We observed that an increase in the charge on the lobe resulted in lobed particles assembling over a wider range of temperatures. We also observed that the lobed particles with charges self-assembled into structures with enhanced porosity in comparison to lobed particles without charges.

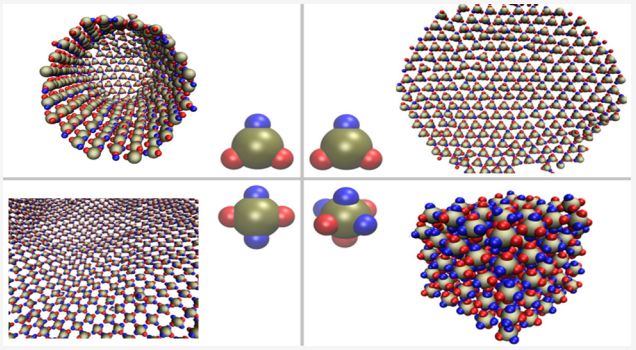

INTRODUCTION

Self-assembly of colloidal particles into structures with desired functional properties is an emerging approach for the discovery of novel materials.[1] One of the strategies to design colloidal particles for self-assembly is to anisotropically decorate the surface of particles with patches made up of synthetic or biological molecules, including proteins[2−4] or complementary DNA strands,[5−9] which result in selective and directional interactions,[10] to provide control over the morphologies of self-assembled structures.[11]

The size, number, location, and interactions among the patches as well as environmental conditions (temperature and concentration) determine the phase behavior and morphology of highly ordered structures.[12] The synthesis of colloidal particles with protrusions (lobes) that mimic atomic valence (i.e., the positions of their lobes resemble hybridized atomic orbitals) results in particles with well-controlled three-dimensional bonding symmetries, which expand the possibilities for novel self-assembled structures.[13] We have previously shown that colloidal particles with lobes self-assemble to form porous structures due to the increased excluded volume created by lobes in their nonspherical shapes.[12,14]

In addition to particle shape and short-range interactions, the charges on colloidal particles also play a key role in determining the phase behavior of self-assembled structures.[15] When working with the self-assembly of oppositely charged colloidal particles, it is crucial to manage the balance between entropically driven close-packed arrangements and electrostatically driven non-close-packed conformations.[16] Rugge et al.[17] tuned the charge on the surface of silica particles and modified ionizable polysterene particles by changing the pH of the solution and showed that they form polycrystalline close-packed arrays when both particles are highly charged. However, when only the silica particles are highly charged, these particles acted as templating agents forcing the weakly interacting polystyrene particles to order into a crystalline lattice.

Tuning of electrostatic interactions between oppositely charged colloidal particles leads to the formation of colloidal crystals,[18] and the changes in the magnitude of these opposite charges result in the formation of different crystal arrangements.[19] Leunissen et al.[18] tuned the charges on the surface of poly(methyl methacrylate) (PMMA) and silica spheres by varying the salt concentration in the suspension and obtained assemblies mimicking NaCl and other binary crystals for different volume fractions and particle sizes. Bartlett et al.[19] observed that changing the magnitude of the charges on the surface of PMMA particles containing different ionizable dyes

Received: December 12, 2020
Revised: February 18, 2021
Published: March 18, 2021

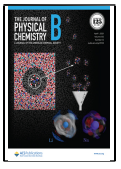

https://doi.org/10.1021/acs.jpcb.0c11096
J. Phys. Chem. B 2021, 125, 3208–3215

led to the formation of different lattices (e.g., face-centered cubic).

Given the importance of long-range interactions, the role of heterogeneously charged patchy particles (i.e., particles with patches of the opposite charge) in the formation of self-assembled structures has been examined.[20,21] Recent developments have allowed the experimental synthesis of colloids with a positively charged equatorial belt and two negatively charged polar patches,[22] and colloids with two oppositely charged patches.[23]

While these experimental studies showed the effect of charges in altering the self-assembled morphology, several previous studies have been limited to charges on the surface of spherical particles. However, no self-assembly studies to date have been performed to understand the role of incorporating charges on the lobes in lobed patchy particles. The use of molecular simulation methods to model and optimize the self-assembly of charged particles is increasingly becoming routine in understanding conditions under which the balance between the entropic and electrostatic contributions can be tuned to produce highly porous structures[12,14,24] and bicontinuous gels.[25−27] In this study, we investigated the effect of incorporating charges on the lobes in lobed patchy particles, characterized the morphologies and porosities of self-assembled structures, and compared the results with our previous study involving lobed particles without charges.[14]

MODELS AND METHODS

Modeled Lobed Particles. We have studied the self-assembly behavior of five different types of lobed particles with charges on the lobes. Based on their shapes, these include trigonal planar (S_3^{TP}), square planar (S_4^{SP}), tetrahedral (S_4^{TH}), trigonal bipyramidal (S_5^{TB}), and octahedral (S_6^{OC}) particles (Figure 1).

We used harmonic potentials to model all bonds (eq 1) and angles (eq 2) in lobed particles with the values of force constants (k_{bond} and k_{angle}) as 1000 (in reduced units) to retain the modeled shapes of particles during simulations.

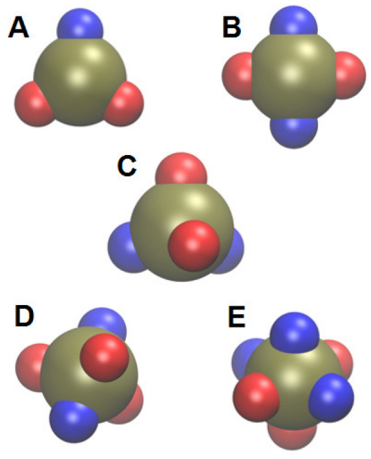

Figure 1. Shapes of charged lobed particles. The neutral central seed particle and the negatively and positively charged lobes are represented by tan, red, and blue spheres, respectively. (A) Trigonal planar (S_3^{TP}), (B) square planar (S_4^{SP}), (C) tetrahedral (S_4^{TH}), (D) trigonal bipyramidal (S_5^{TB}), and (E) octahedral (S_6^{OC}).

$$V_{bond}(r_{ij}) = \frac{1}{2}k_{bond}(r_{ij} - r_0)^2 \quad (1)$$

$$V_{angle}(\theta_{ijk}) = \frac{1}{2}k_{angle}(\theta_{ijk} - \theta_0)^2 \quad (2)$$

The parameter r_{ij} is the distance between the particles i and j, θ_{ijk} is the angle formed between the particles i, j, and k, and r_0 and θ_0 are the equilibrium bond distance and angle, respectively.

All parameters used in our simulations had reduced units. The diameters of a seed (σ_S) and a lobe (σ_L) were set as 2 and 1, respectively. The mass of each seed (m_S) and lobe (m_L) was set as 1. We considered three different types of charges for the negative lobes: −2.0, −4.0, and −6.0. We ensured that the overall charge of each lobed particle was neutral per eq 3

$$|q_{PL}| = \frac{N_{NL}|q_{NL}|}{N_{PL}} \quad (3)$$

where q_{PL} and q_{NL} are the charges in the positive and negative lobes, respectively, and N_{PL} and N_{NL} are the number of positive and negative lobes present in each particle, respectively. Taking a four-lobed square planar (S_4^{SP}) particle as an example, where two lobes are negative and two lobes are positive, if each of its two negative lobes has a −2.0 charge, then each of its two positive lobes will have a +2.0 charge. However, in a five-lobed trigonal bipyramidal (S_5^{TB}) particle, where three lobes are negative and two lobes are positive, if each of its three negative lobes has a −2.0 charge, then the remaining two positive lobes will have a +3.0 charge each.

Interaction Potentials. The nonbonded interactions between seed−seed (S−S), lobe−lobe (L−L), and seed−lobe (S−L) pairs were modeled by using the shifted Lennard-Jones (SLJ) potential (eq 4)

$$V_{SLJ}(r_{ij}) = 4\varepsilon_{ij}\left[\left(\frac{\sigma}{r_{ij} - \Delta}\right)^{12} - \left(\frac{\sigma}{r_{ij} - \Delta}\right)^{6}\right] \quad (4)$$

where ε_{ij} is the depth of the pair-potential well for species i and j and σ is the diameter of the particle. Equation 4 was used to model the pairwise interactions when $r_{ij} < r_{cut} + \Delta$, where r_{cut} is a cutoff distance and $\Delta = (\sigma_i + \sigma_j)/2 - 1$, where σ_i and σ_j are the diameters of the particles i and j, respectively. When $r_{ij} \geq (r_{cut} + \Delta)$, nonbonded interactions are neglected, i.e., $V_{SLJ}(r_{ij}) = 0$. The electrostatic interactions that arise due to the charged lobes were accounted for by using an electrostatic potential (eq 5)

$$V_{Elec}(r_{ij}) = \frac{q_i q_j}{4\pi\varepsilon_0\varepsilon_r}\frac{1}{r_{ij}} \quad (5)$$

where q_i and q_j are the charges on the particles i and j, respectively, and ε_0 and ε_r are the permittivity of the free space and the relative permittivity, respectively. To account for electrostatic screening, ε_r represents the dielectric permittivity of bulk water (equal to 80) at ambient conditions.

Simulation Details. Coarse-grained Langevin dynamics simulations were performed for each system by using HOOMD-Blue, a GPU-accelerated molecular dynamics (MD) software package.[28] All potentials used to model nonbonded interactions were implemented in HOOMD-Blue. The electrostatic interactions were modeled by using the particle−particle−particle-mesh (PPPM) method.[29,30]

https://doi.org/10.1021/acs.jpcb.0c11096
J. Phys. Chem. B 2021, 125, 3208−3215

Each system was composed of 15625 particles of the same type, and the length of the simulation domain along each direction was $200\sigma_L$. The initial configuration of particles for each system was randomized by simulating them for 10^4 steps at k_BT = 3.0, a temperature high enough to prevent self-assembly at all conditions.

The depth of the interatomic potential for the negative lobe−positive lobe (NL−PL) pairs was fixed at 3, while for all the other pairs it was set as 1. The short-ranged repulsive interactions were modeled by setting the cutoff distance (r_{cut}) as $2^{1/6}\sigma$ in the SLJ potential for all pairs other than the NL−PL pairs, since the interactions between NL−PL pairs are attractive. For the NL−PL pairs, we used $r_{cut} = 2.5\sigma$ to ensure attractive interactions. The σ values in the SLJ potential were set to 2.0, 1.5, and 1.0 for the S−S, S−L, and L−L pairs, respectively. All parameters for the interatomic potential have dimensionless units, and their values were chosen for consistency with our previous work.[14]

We performed simulations of all five types of particles at eight different temperature conditions: k_BT = 0.1, 0.3, 0.5, 0.7, 0.9, 1.1, 1.3, and 1.5 (which translates into a temperature range of 29.8−447.0 K, based on the same mapping conditions described by Long and Ferguson[31]) for each charge value (−2.0, −4.0, and −6.0), hence a total of 120 simulations. Depending on the number of lobes attached to the seed, the volume fraction (Φ) of the lobed particles in simulation domains varied from 0.010 to 0.011, per eq 6.

$$\Phi = \frac{N(V_C + N_L V_L)}{V_0} \tag{6}$$

where N is the number of particles in the system, N_L is the number of lobes in the particle, V_C is the volume of the central seed particle, V_L is the volume of a single lobe, and V_0 is the volume of the simulation box.

We also performed 10 additional simulations (two for each type of particle) to investigate the effect of changing Φ on the morphology of self-assembled structures by varying Φ between 0.010 and 0.078. The conditions of temperature and lobe charges for these additional simulations were the ones that caused the formation of the largest self-assembled structures in simulations using the original volume fractions. All systems were simulated by using a time step of 0.005 for 5×10^7 steps to allow the self-assembled structures to reach equilibrium.

Morphology Analysis. The radial distribution function (RDF) for the seed−seed pair was calculated via eq 7

$$g(r) = \frac{\rho(r)}{\rho_0} \tag{7}$$

where $\rho(r)$ is the density of particles at a distance r from the reference particle and ρ_0 is the bulk density. Based on the RDF curves and qualitative visual inspections using the VMD software,[32] we have identified six different types of self-assembled phases: chains (CH), crystalline structures (CR), liquid droplets (LD), random aggregates (RA), spherical aggregates (SA), and two-dimensional sheets (SH).

In random aggregates, there is no order between the seeds, and they represent a diverse set of shapes (e.g., cylinders and wires). The spherical aggregates also do not reveal significant order between the seeds although they have a well-defined spherical shape. We define liquid droplets as those self-assembled structures that show well-defined second and third coordination shells, as identified by the presence of one or two broad peaks following the first intense peak (first coordination shell) in the RDF. The crystalline structures are those where the seeds are well-ordered, as indicated by the RDF showing several intense peaks at regular intervals. The names given to the remaining structures are chains and two-dimensional sheets.

Porosity Analysis. We extracted the largest possible cuboids from the self-assembled structures and used the Zeo ++ software[33−35] to compute the pore size distributions (PSD) and accessible surface area (ASA) and to estimate the diameter of the largest free sphere (D_{LFS}), which is the largest sphere that can freely diffuse through a self-assembled porous structure. For the PSD and ASA calculations, we have used a probe radius equivalent to $^1/_2\sigma_L$, consistent with our previous work.[14]

RESULTS

We observed that the equilibrium phase was reached for all conditions where the self-assembly occurred, as confirmed by the convergence of the potential energy per particle (Figure S1). To gain a better understanding of the phase behavior for each type of particle, we first report the overall morphologies of all self-assembled structures as a function of temperature and charge (Figure 2). The morphologies were assigned based on the RDF of each system (Figure S2) and visual inspection. For each type of particle, we observed self-assembly at a wide range of temperature conditions with an increase in the charge on each lobe and thereby increased electrostatic interactions between the lobes.

For example, in Figure 2A we depict the phase behavior of trigonal planar (S_3^{TP}) particles for all simulated conditions. These particles were observed to self-assemble into random aggregates (RA1) at lower temperatures. With an increase in the charge on the lobes, we observed a morphological transition to spherical aggregates (SA at $q_{NL} = -4.0/k_BT = 0.7$) and two-dimensional sheets (SH at $q_{NL} = -4.0/k_BT = 0.5$ and at $q_{NL} = -6.0/k_BT = 0.3-1.3$). The formation of chains (CH) was observed at $q_{NL} = -2.0/k_BT = 0.3$. Most of these chains are bent, without branches, and composed of 4−30 particles (Figure S3). The longest chain in this phase is composed of 692 particles (Figure S4).

We note that the random aggregates of S_3^{TP} particles formed at lower temperatures (termed RA1), at moderate temperatures (termed RA2), and at higher temperatures (termed RA3) are distinct from each other. In RA1, a mixture of chains, two-dimensional sheets, and three-dimensional aggregates was observed (Figure S5A). However, RA2 is composed of only three-dimensional aggregates (Figure S5B), and RA3 is composed of sheets that fold and wrap around each other, forming porous three-dimensional aggregates (Figure 3B) and small polyhedra-like hollow structures (Figure 3C), where no particles inside the external shell exist. We performed additional simulations (Figure 3D) and confirmed that these structures originate from the sheets (Figure 3E). We also observed the formation of cylindrical tubes in these independent simulations (Figure 3F).

The square planar (S_4^{SP}) particles formed only one type of self-assembled phase having two-dimensional sheets. For this type of building block, self-assembly was observed only at lower temperatures for $q_{NL} = -2.0$, at lower to moderate temperatures for $q_{NL} = -4.0$, and up to higher temperatures when $q_{NL} = -6.0$ (Figure 2B).

https://doi.org/10.1021/acs.jpcb.0c11096
J. Phys. Chem. B 2021, 125, 3208−3215

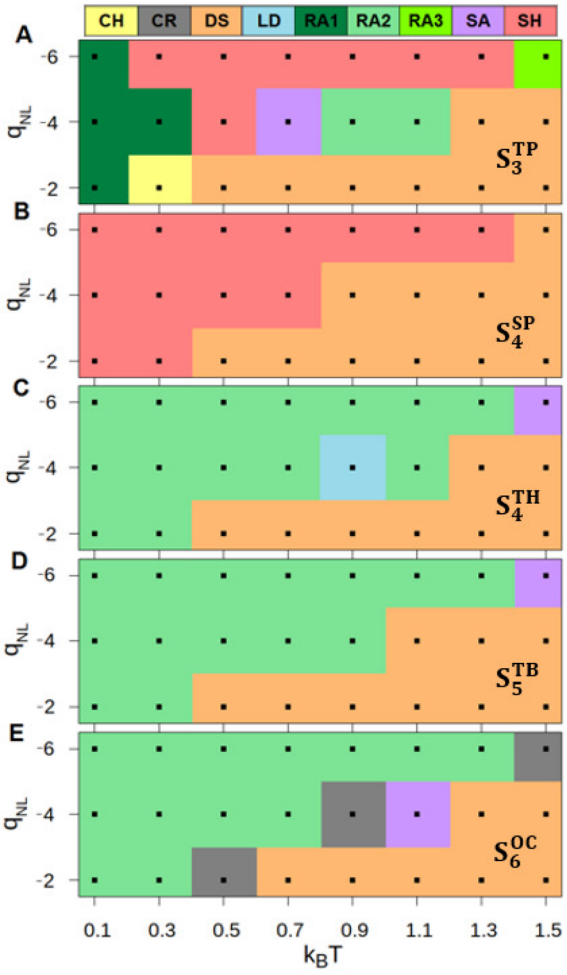

Figure 2. Phase behavior and morphologies of self-assembled lobed particles: (A) trigonal planar (S_3^{TP}), (B) square planar (S_4^{SP}), (C) tetrahedral (S_4^{TH}), (D) trigonal bipyramidal (S_5^{TB}), and (E) octahedral (S_6^{OC}). Labels: CH, CR, DS, LD, SA, and SH denote chains, crystalline state, dissociated state (no self-assembly), liquid droplets, spherical aggregates, and 2-dimensional sheets, respectively. RA1, RA2, and RA3 denote three different types of random aggregates.

While a variation in the temperature of the system did not change the type of self-assembled structures (Figure 2B), it played a role in the overall size of two-dimensional sheets (Figure 4A,B). By increasing the temperature of the system

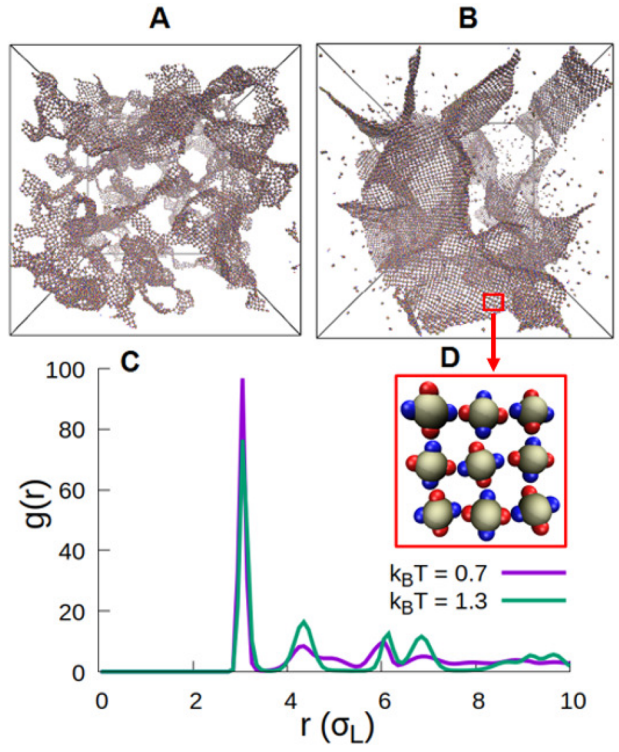

Figure 4. Self-assembly of square planar particles under different temperature conditions. (A) Smaller sheets (k_BT = 0.7). (B) Larger sheets (k_BT = 1.3). (C) RDF curves for self-assembled structures shown in panels A and B. (D) Structural motif observed in two-dimensional sheets (central seeds appear to have different sizes due to the curvature in sheets).

from k_BT = 0.7 to 1.3 and having the charges on the lobes fixed with q_{NL} = −6, the smaller sheets gradually merged together to form larger two-dimensional sheets (Figure 4A,B), while maintaining their structural motif (Figure 4D). This effect

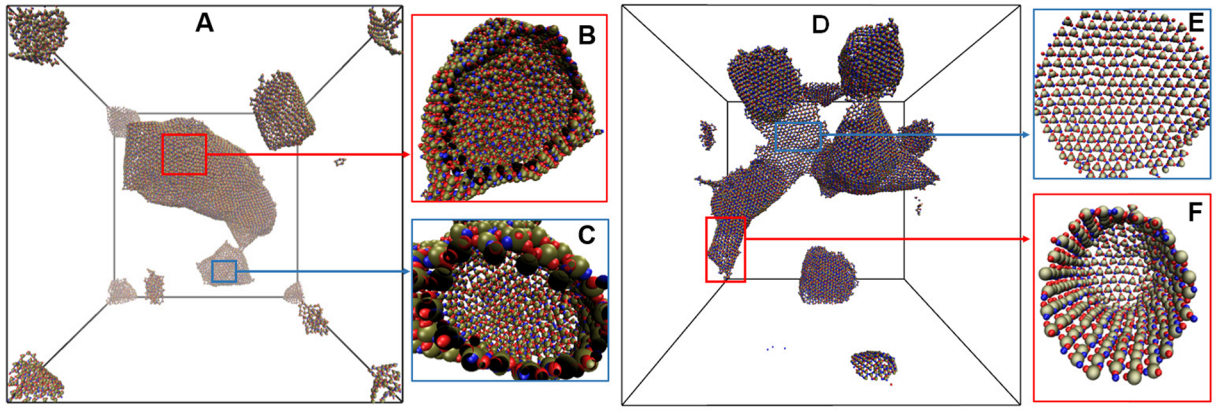

Figure 3. Morphology comparison between independent simulations of trigonal planar particles. The conditions that led to RA3 formation (q_{NL} = −6.0/k_BT = 1.5) were simulated by using new randomized initial positions to confirm that the structures observed originate from the sheets. (A) A snapshot of the simulation domain from the end of the simulation with the original randomized initial positions. (B, C) A cross-sectional view of the porous and hollow RA3-type structures, respectively. (D) A snapshot of the simulation domain from the end of the simulation with the new randomized positions. (E, F) A cross-sectional view of a two-dimensional sheet and a cylindrical tube, respectively.

https://doi.org/10.1021/acs.jpcb.0c11096
J. Phys. Chem. B 2021, 125, 3208−3215

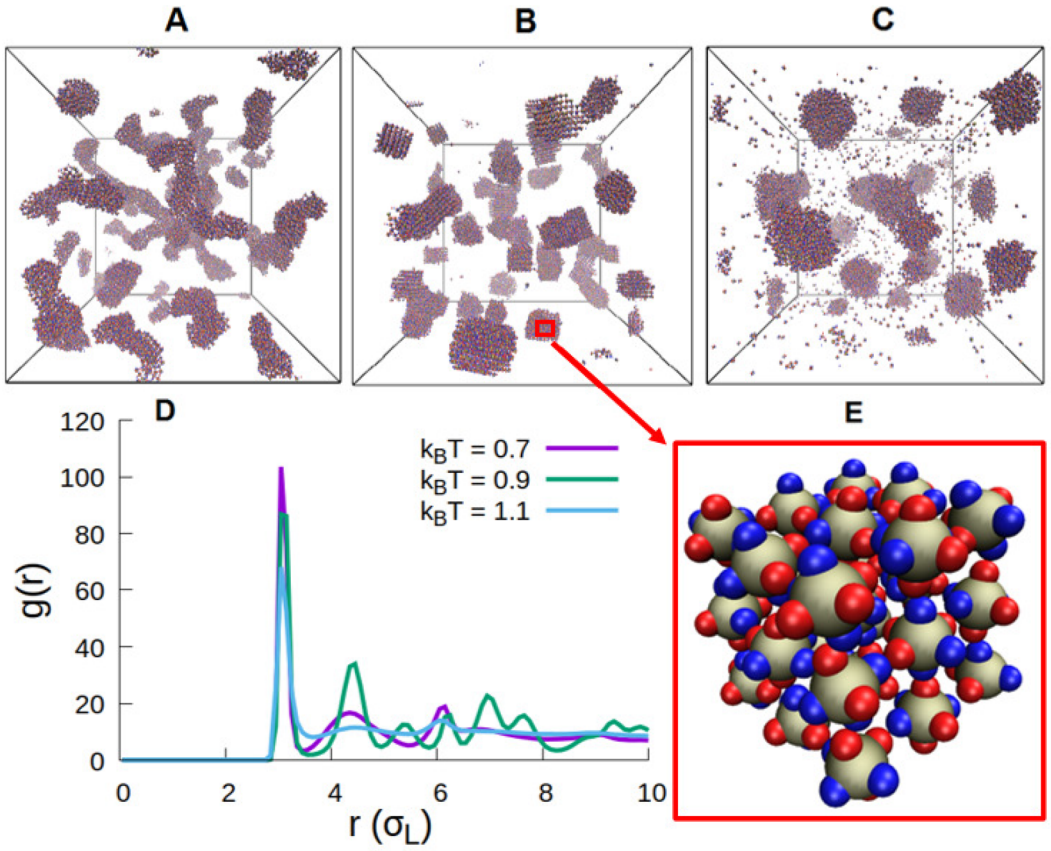

Figure 5. Phase transition observed in systems composed of octahedral particles. The self-assembled morphology transitions from (A) random aggregates (RA2) to (B) crystalline (CR) structures and then transitions again to (C) spherical aggregates (SA). (D) RDF curves for the structures involved in the phase transitions. (E) A unit cell of the crystalline structures formed by the S_6^{OC} particles.

can also be observed by comparing the RDF for self-assembled structures, as the RDF curve for k_BT = 1.3 shows a higher density of lobed particles in the second, third, and fourth coordination shells (Figure 4C).

We note that both S_3^{TP} and S_4^{SP} particles formed large two-dimensional sheets (Figure S6) with similar sizes (14797 and 14426 particles for S_3^{TP} and S_4^{SP}, respectively) at the same condition (q_{NL} = −6.0/k_BT = 1.3), but their morphology is different. The sheets formed by S_3^{TP} particles show a triangular structural motif, where each pore is surrounded by three particles (Figure S6C), while the sheets formed by S_4^{SP} particles show a square structural motif, where each pore is bounded by four particles (Figure S6D).

For the tetrahedral (S_4^{TH}) particles, simulations showed that self-assembly occurs only for k_BT = 0.1 and 0.3 when q_{NL} = −2.0, for the range of k_BT = 0.1−0.9 when q_{NL} = −4.0, and for all temperature conditions investigated when q_{NL} = −6.0. It was also observed that the formation of random aggregates (RA2) occurred for most conditions where self-assembly phenomena were observed (Figure 2C). The exceptions were the transitions from random aggregates (RA2) to liquid droplets (LD) at k_BT = 0.9 and q_{NL} = −4.0 and from random aggregates (RA2) to spherical aggregates (SA) at k_BT = 1.5 and q_{NL} = −6.0.

The phase behavior of trigonal bipyramidal (S_5^{TB}) particles (Figure 2D) is similar to that of the S_4^{TH} particles (Figure 2C), with the exception that there was no formation of liquid droplets (LD) at any conditions and no self-assembly for q_{NL} = −4.0 occurred beyond k_BT = 0.9.

The octahedral (S_6^{OC}) particles self-assembled within the range of k_BT = 0.1−0.5, k_BT = 0.1−1.1, and k_BT = 0.1−1.5 when q_{NL} = −2.0, −4.0, and −6.0, respectively (Figure 2E). While random aggregates (RA2) were formed for most simulation conditions, S_6^{OC} particles also formed crystalline (CR) structures under three different conditions: k_BT = 0.5 and q_{NL} = −2.0, k_BT = 0.9 and q_{NL} = −4.0, and k_BT = 1.5 and q_{NL} = −6.0. The octahedral particles were the only charged lobed particles to self-assemble into crystalline structures under the conditions investigated in this study.

Specifically, at q_{NL} = −4.0, we observed that the S_6^{OC} particles undergo a phase transition from random aggregates (RA2) (Figure 5A) to crystalline (CR) structures (Figure 5B) at k_BT = 0.9, then another transition from crystalline (CR) structures to spherical aggregates (SA) (Figure 5C) occurs at k_BT = 1.1. We hypothesize that this transition occurs due to a delicate balance between the electrostatic interactions and the diffusion effects that are dependent on the temperature of the system. To form crystalline structures, the particles need just sufficient kinetic energy to diffuse and adjust their positions for the growth of the crystalline lattice. However, at a lower temperature (k_BT = 0.7), the particles do not diffuse sufficiently due to a decreased kinetic energy, while at a higher temperature (k_BT = 1.1), their kinetic energy is too high and they begin to disassemble. The RDF curve for the condition when q_{NL} = −4.0 and k_BT = 0.9 shows a series of well-defined and regularly spaced peaks, confirming the crystalline nature of the self-assembled structures (Figure 5D). The arrangement of

https://doi.org/10.1021/acs.jpcb.0c11096
J. Phys. Chem. B 2021, 125, 3208−3215

particles in a cubic unit cell of the crystalline self-assembled structures is also shown in Figure 5E.

We observed the formation of spherical aggregates for four different types of particles at the following conditions: S_3^{TP} ($q_{NL} = -4.0/k_BT = 0.7$), S_4^{TH} ($q_{NL} = -6.0/k_BT = 1.5$), S_5^{TB} ($q_{NL} = 6.0/k_BT = 1.5$), and S_6^{OC} ($q_{NL} = -4.0/k_BT = 1.1$). In Figure S7, we show the largest spherical cluster observed for each of the four types of particles. These data reveal that the number of particles in spherical aggregates decreases as the number of lobes on the particles increases. The spherical aggregates range from 3820 particles for the S_3^{TP} system to 1196 particles for the S_6^{OC} system.

To characterize porosities of self-assembled structures, the largest possible cuboids were extracted from the three-dimensional structures formed by self-assembly of each type of particle, with the exception of S_4^{SP} particles, which only showed two-dimensional sheets. The pore size distributions (Figure 6) showed that S_5^{TB} and S_6^{OC} self-assemble to form

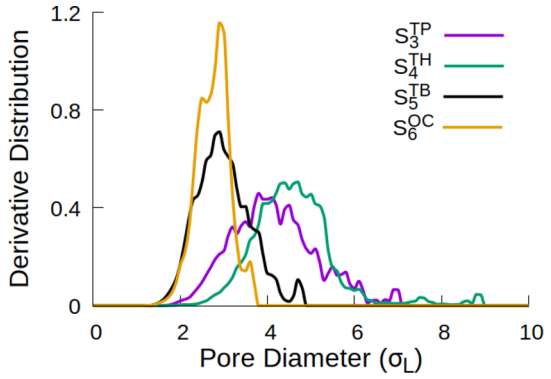

Figure 6. Pore size distributions. The PSD curves for three-dimensional porous structures formed by self-assembly of trigonal planar, tetrahedral, trigonal bipyramidal, and octahedral particles. The distribution for square-planar particles is not shown due to their self-assembly into two-dimensional sheets.

structures with more homogeneous and smaller pores (ranging between $1.5\sigma_L$ to $4.5\sigma_L$, and between $1.5\sigma_L$ to $3.7\sigma_L$, respectively), as indicated by a sharp peak in the distributions. This is likely due to a higher number of lobes, which results in well packed structures. However, structures formed via self-assembly of S_3^{TP} and S_4^{TH} particles were observed to be more heterogeneous and having larger pores (ranging between $2.5\sigma_L$ to $6.5\sigma_L$, and between $2.0\sigma_L$ to $6.2\sigma_L$, respectively).

We also estimated the ASA (Figure S8) by using the cuboids extracted from self-assembled structures and observed that the particles with the most lobes (S_5^{TB} and S_6^{OC}) provided structures with a higher and comparable ASA, as expected based on the higher surface area of the individual particles. However, we also observed that the structures formed by the S_4^{TH} particles showed a significantly lower ASA than the structures formed by S_3^{TP}. This occurs because the structures formed by the S_3^{TP} particles are more packed than the ones formed by the S_4^{TH} particles (Figure 6) since they originate from a collection of two-dimensional sheets folded and wrapped around each other (Figure 3).

We also investigated the effect of varying the volume fraction of particles (Φ) on observed self-assembled morphologies (Figure 7). These data indicate that for most of the particles variations in Φ did not affect the type of morphology observed. In fact, increasing Φ resulted in more uniform and large-scale

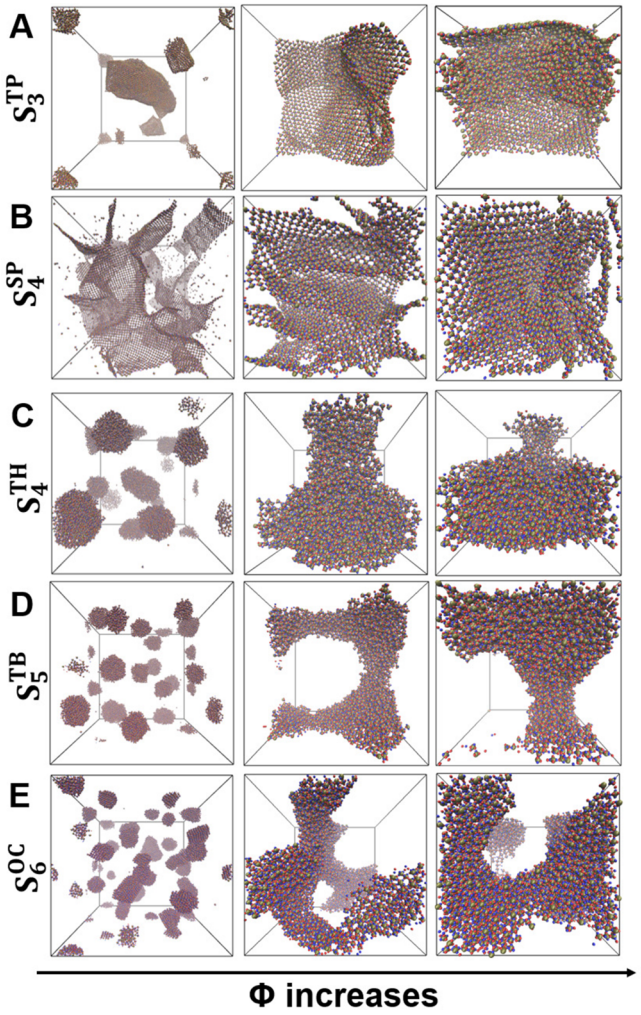

Figure 7. Snapshots of simulation domains at various volume fractions (Φ): (A) trigonal planar (Φ = 0.010, 0.040, and 0.067), (B) square planar (Φ = 0.010, 0.042, and 0.071), (C) tetrahedral (Φ = 0.010, 0.042, and 0.071), (D) trigonal bipyramidal (Φ = 0.011, 0.044, and 0.074), and (E) octahedral (Φ = 0.011, 0.046, and 0.078).

self-assembled structures. This observation is consistent with the results from our previous work on particles without charges.[14] The only exception was the S_6^{OC} particles, where an increase in Φ resulted in a change in the morphology observed (from crystalline at Φ = 0.011 to random aggregates at Φ = 0.046 and 0.078) (Figure 7E). This occurs because the higher densities are a limiting factor for the diffusion of the particles required for the formation of the crystalline lattices.

DISCUSSION

In this work, we investigated the effect of adding charges to lobes on lobed colloidal particles. We observed a direct correlation between the formation of self-assembled structures and the magnitude of charges on the lobes, where an increase in the charge on a lobe led to self-assembly at a wider range of temperatures. We also observed that the volume fraction (Φ) did not have an influence on the type of morphology of a self-assembled structure although larger self-assemblies were observed on increasing Φ. Here, we compare the results obtained for simulations of the lobed particles with charges and those from our simulations of lobed particles without charges that were reported in our previous work.[14]

https://doi.org/10.1021/acs.jpcb.0c11096
J. Phys. Chem. B 2021, 125, 3208−3215

In our earlier work,[14] lobed particles without charges were subjected to short-range interactions that led to several morphologies (e.g., sheets, tubes, clathrates, polyhedra, face-centered cubic lattices, and hexagonal close-packed structures). However, as reported in this work, lobed particles with charges on the lobes did not form many structures showing a long-range order. The only exceptions were the two-dimensional sheets formed by S_3^{TP} and S_4^{SP} particles and the simple cubic crystals formed by S_6^{OC} particles for certain conditions (Figure 2).

We also compared the porosity of self-assembled structures obtained from lobed particles with and without charges. We chose the diameter of the largest free sphere (D_{LFS}) as the metric for porosity comparison, since a higher porosity and the formation of a network of pores are desirable characteristics for materials with applications in several fields, including tissue engineering.[36] A comparison of morphologies of uncharged and charged particles is shown in Table S1, and their RDFs are shown in Figure S9.

The estimates for D_{LFS} showed that the lobed particles with charges reveal morphologies that are more porous than the ones formed by lobed particles without charges (Figure 8).

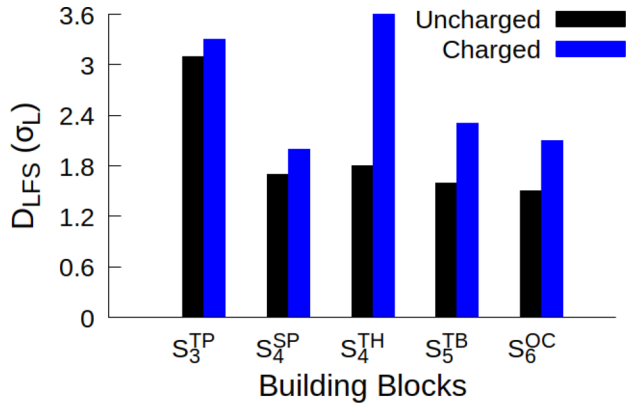

Figure 8. Diameter of the largest free sphere (D_{LFS}). A comparison of porosity, as measured by D_{LFS}, is shown for uncharged and charged lobed particles. Data for uncharged particles are from our previous work.[14]

This likely happens due to the repulsive electrostatic interactions that arise between the lobes having the same charges, an effect that is not observed when the lobes are without charges and lacking electrostatic interactions.

We have observed that the structures formed via self-assembly of S_4^{TH} particles showed the highest porosity among those investigated in this study ($D_{LFS} = 3.6\sigma_L$). However, S_4^{SP}, S_5^{TB}, and S_6^{OC} particles formed the least porous structures due to a tighter packing that occurs when two-dimensional structures are formed (in the case of S_4^{SP} particles) and when the particles have a higher number of lobes (in the case of S_5^{TB} and S_6^{OC} building blocks).

To find suitable applications in tissue engineering, a three-dimensional scaffold is expected to mimic the heterogeneous and porous nature of the extracellular matrix (ECM) as well as provide the mechanical strength needed for keeping its integrity while the tissue regenerates.[37] To mimic the ECM, scaffolds used for tissue regeneration must have a structure with interconnected pores and high porosity, allowing cellular penetration and nutrient diffusion with minimal constraints.[38]

The higher porosities and more heterogeneous character of our structures, especially the ones formed by self-assembly of S_3^{TP} and S_4^{TH} particles, indicate that the particles with charged lobes should be more suitable for designing materials with applications in the field of tissue engineering.[39] Furthermore, the electrostatic interactions that arise in the particles with charged lobes produce structures that likely have a higher mechanical stability than the ones produced by weakly interacting particles having only short-range interactions due to uncharged lobes. We also note that the shapes of most particles (except square planar) are experimentally realizable,[13,40−43] but new strategies need to be developed to site-specifically functionalize lobes in experiments.

■ ASSOCIATED CONTENT

Supporting Information

The Supporting Information is available free of charge at https://pubs.acs.org/doi/10.1021/acs.jpcb.0c11096.

Figures S1−S9 and Table S1 (PDF)

■ AUTHOR INFORMATION

Corresponding Author

Harish Vashisth − *Department of Chemical Engineering, University of New Hampshire, Durham, New Hampshire 03824, United States;* orcid.org/0000-0002-2087-2880; Phone: +1-603-862-2483; Email: harish.vashisth@unh.edu; Fax: +1-603-862-3747

Authors

Brunno C. Rocha − *Department of Chemical Engineering, University of New Hampshire, Durham, New Hampshire 03824, United States*

Sanjib Paul − *Department of Chemistry, New York University, New York City, New York 10003, United States*

Complete contact information is available at: https://pubs.acs.org/10.1021/acs.jpcb.0c11096

Notes

The authors declare no competing financial interest.

■ ACKNOWLEDGMENTS

We gratefully acknowledge the financial support provided by the National Science Foundation (NSF) EPSCoR award (OIA-1757371; H.V.). We also acknowledge computational support through BioMade, a heterogeneous CPU/GPU cluster at the University of New Hampshire supported by the NSF EPSCoR award (OIA-1757371; H.V.).

■ REFERENCES

(1) Glotzer, S. C. Materials science. Some assembly required. *Science* **2004**, *306*, 419−420.

(2) Chervyachkova, E.; Wegner, S. V. Reversible social self-sorting of colloidal cell-mimics with blue light switchable proteins. *ACS Synth. Biol.* **2018**, *7*, 1817−1824.

(3) Gurunatha, K. L.; Fournier, A. C.; Urvoas, A.; Valerio-Lepiniec, M.; Marchi, V.; Minard, P.; Dujardin, E. Nanoparticles self-assembly driven by high affinity repeat protein pairing. *ACS Nano* **2016**, *10*, 3176−3185.

(4) Obana, M.; Silverman, B. R.; Tirrell, D. A. Protein-Mediated Colloidal Assembly. *J. Am. Chem. Soc.* **2017**, *139*, 14251−14256.

(5) Rogers, W. B.; Shih, W. M.; Manoharan, V. N. Using DNA to program the self-assembly of colloidal nanoparticles and micro-particles. *Nat. Rev. Mater.* **2016**, *1*, 16008.

(6) Biancaniello, P. L.; Kim, A. J.; Crocker, J. C. Colloidal interactions and self-assembly using DNA hybridization. *Phys. Rev. Lett.* **2005**, *94*, 058302.
(7) Valignat, M.-P.; Theodoly, O.; Crocker, J. C.; Russel, W. B.; Chaikin, P. M. Reversible self-assembly and directed assembly of DNA-linked micrometer-sized colloids. *Proc. Natl. Acad. Sci. U. S. A.* **2005**, *102*, 4225−4229.
(8) Nykypanchuk, D.; Maye, M. M.; van der Lelie, D.; Gang, O. DNA-guided crystallization of colloidal nanoparticles. *Nature* **2008**, *451*, 549−552.
(9) Shyr, M. H. S.; Wernette, D. P.; Wiltzius, P.; Lu, Y.; Braun, P. V. DNA and DNAzyme-mediated 2D colloidal assembly. *J. Am. Chem. Soc.* **2008**, *130*, 8234−8240.
(10) Zhang, Z.; Glotzer, S. C. Self-assembly of patchy particles. *Nano Lett.* **2004**, *4*, 1407−1413.
(11) Kraft, D. J.; Groenewold, J.; Kegel, W. K. Colloidal molecules with well-controlled bond angles. *Soft Matter* **2009**, *5*, 3823.
(12) Paul, S.; Vashisth, H. Self-assembly behavior of experimentally realizable lobed patchy particles. *Soft Matter* **2020**, *16*, 8101−8107.
(13) Wang, Y.; Wang, Y.; Breed, D. R.; Manoharan, V. N.; Feng, L.; Hollingsworth, A. D.; Weck, M.; Pine, D. J. Colloids with valence and specific directional bonding. *Nature* **2012**, *491*, 51−55.
(14) Paul, S.; Vashisth, H. Self-assembly of lobed particles into amorphous and crystalline porous structures. *Soft Matter* **2020**, *16*, 1142−1147.
(15) Rosenberg, M.; Dekker, F.; Donaldson, J. G.; Philipse, A. P.; Kantorovich, S. S. Self-assembly of charged colloidal cubes. *Soft Matter* **2020**, *16*, 4451−4461.
(16) Li, F.; Josephson, D. P.; Stein, A. Colloidal assembly: the road from particles to colloidal molecules and crystals. *Angew. Chem., Int. Ed.* **2011**, *50*, 360−388.
(17) Rugge, A.; Tolbert, S. H. Effect of electrostatic interactions on crystallization in binary colloidal films. *Langmuir* **2002**, *18*, 7057−7065.
(18) Leunissen, M. E.; Christova, C. G.; Hynninen, A.-P.; Royall, C. P.; Campbell, A. I.; Imhof, A.; Dijkstra, M.; van Roij, R.; van Blaaderen, A. Ionic colloidal crystals of oppositely charged particles. *Nature* **2005**, *437*, 235−240.
(19) Bartlett, P.; Campbell, A. I. Three-dimensional binary superlattices of oppositely charged colloids. *Phys. Rev. Lett.* **2005**, *95*, 128302.
(20) Dempster, J. M.; Olvera de la Cruz, M. Aggregation of heterogeneously charged colloids. *ACS Nano* **2016**, *10*, 5909−5915.
(21) Noya, E. G.; Kolovos, I.; Doppelbauer, G.; Kahl, G.; Bianchi, E. Phase diagram of inverse patchy colloids assembling into an equilibrium laminar phase. *Soft Matter* **2014**, *10*, 8464−8474.
(22) Bianchi, E.; van Oostrum, P. D.; Likos, C. N.; Kahl, G. Inverse patchy colloids: Synthesis, modeling and self-organization. *Curr. Opin. Colloid Interface Sci.* **2017**, *30*, 8−15.
(23) Mehr, F. N.; Grigoriev, D.; Heaton, R.; Baptiste, J.; Stace, A. J.; Puretskiy, N.; Besley, E.; Böker, A. Self-assembly behavior of oppositely charged inverse bipatchy microcolloids. *Small* **2020**, *16*, 2000442.
(24) Cerbelaud, M.; Videcoq, A.; Abélard, P.; Pagnoux, C.; Rossignol, F.; Ferrando, R. Self-assembly of oppositely charged particles in dilute ceramic suspensions: predictive role of simulations. *Soft Matter* **2010**, *6*, 370−382.
(25) Schmidle, H.; Hall, C. K.; Velev, O. D.; Klapp, S. H. L. Phase diagram of two-dimensional systems of dipole-like colloids. *Soft Matter* **2012**, *8*, 1521−1531.
(26) Goyal, A.; Hall, C. K.; Velev, O. D. Self-assembly in binary mixtures of dipolar colloids: Molecular dynamics simulations. *J. Chem. Phys.* **2010**, *133*, 064511.
(27) Goyal, A.; Hall, C. K.; Velev, O. D. Bicontinuous gels formed by self-assembly of dipolar colloid particles. *Soft Matter* **2010**, *6*, 480−484.
(28) Anderson, J. A.; Glaser, J.; Glotzer, S. C. HOOMD-blue: A Python package for high-performance molecular dynamics and hard particle Monte Carlo simulations. *Comput. Mater. Sci.* **2020**, *173*, 109363.
(29) Hockney, R.; Goel, S.; Eastwood, J. Quiet high-resolution computer models of a plasma. *J. Comput. Phys.* **1974**, *14*, 148−158.
(30) LeBard, D. N.; Levine, B. G.; Mertmann, P.; Barr, S. A.; Jusufi, A.; Sanders, S.; Klein, M. L.; Panagiotopoulos, A. Z. Self-assembly of coarse-grained ionic surfactants accelerated by graphics processing units. *Soft Matter* **2012**, *8*, 2385−2397.
(31) Long, A. W.; Ferguson, A. L. Nonlinear Machine Learning of Patchy Colloid Self-Assembly Pathways and Mechanisms. *J. Phys. Chem. B* **2014**, *118*, 4228−4244.
(32) Humphrey, W.; Dalke, A.; Schulten, K. VMD-Visual Molecular Dynamics. *J. Mol. Graphics* **1996**, *14*, 33−38.
(33) Willems, T. F.; Rycroft, C. H.; Kazi, M.; Meza, J. C.; Haranczyk, M. Algorithms and tools for high-throughput geometry-based analysis of crystalline porous materials. *Microporous Mesoporous Mater.* **2012**, *149*, 134−141.
(34) Pinheiro, M.; Martin, R. L.; Rycroft, C. H.; Jones, A.; Iglesia, E.; Haranczyk, M. Characterization and comparison of pore landscapes in crystalline porous materials. *J. Mol. Graphics Modell.* **2013**, *44*, 208−219.
(35) Pinheiro, M.; Martin, R. L.; Rycroft, C. H.; Haranczyk, M. High accuracy geometric analysis of crystalline porous materials. *CrystEngComm* **2013**, *15*, 7531.
(36) Chen, G.; Ushida, T.; Tateishi, T. Scaffold design for tissue engineering. *Macromol. Biosci.* **2002**, *2*, 67−77.
(37) Loh, Q. L.; Choong, C. Three-dimensional scaffolds for tissue engineering applications: role of porosity and pore size. *Tissue Eng., Part B* **2013**, *19*, 485−502.
(38) O'Brien, F. J. Biomaterials & scaffolds for tissue engineering. *Mater. Today* **2011**, *14*, 88−95.
(39) Yoo, D.-J. Computer-aided porous scaffold design for tissue engineering using triply periodic minimal surfaces. *Int. J. Precis. Eng. Manuf.* **2011**, *12*, 61−71.
(40) Stubbs, J.; Tsavalas, J.; Carrier, R.; Sundberg, D. The structural evolution of composite latex particles during starve-fed emulsion polymerization: modeling and experiments for kinetically frozen morphologies. *Macromol. React. Eng.* **2010**, *4*, 424−431.
(41) Meester, V.; Verweij, R. W.; van der Wel, C.; Kraft, D. Colloidal recycling: reconfiguration of random aggregates into patchy particles. *ACS Nano* **2016**, *10*, 4322−4329.
(42) Blenner, D.; Stubbs, J.; Sundberg, D. Multi-lobed composite polymer nanoparticles prepared by conventional emulsion polymerization. *Polymer* **2017**, *114*, 54−63.
(43) Gong, Z.; Hueckel, T.; Yi, G.-R.; Sacanna, S. Patchy particles made by colloidal fusion. *Nature* **2017**, *550*, 234−238.

https://doi.org/10.1021/acs.jpcb.0c11096
J. Phys. Chem. B 2021, 125, 3208−3215